

Article

Characterization of Snow Facies on the Greenland Ice Sheet Observed by TanDEM-X Interferometric SAR Data

Paola Rizzoli ^{1,*}, Michele Martone ¹, Helmut Rott ^{2,3} and Alberto Moreira ¹

¹ German Aerospace Center (DLR), Microwaves and Radar Institute, Oberpfaffenhofen, 82234 Weßling, Germany; michele.martone@dlr.de (M.M.); alberto.moreira@dlr.de (A.M.)

² ENVEO IT GmbH, Technikerstrasse 21a, A-6020 Innsbruck, Austria; Helmut.Rott@uibk.ac.at

³ Institute of Atmospheric and Cryospheric Sciences, University of Innsbruck, A-6020 Innsbruck, Austria

* Correspondence: paola.rizzoli@dlr.de; Tel.: +49-8153-28-1785

Academic Editors: Xiaofeng Li and Prasad S. Thenkabail

Received: 18 January 2017; Accepted: 24 March 2017; Published: 28 March 2017

Abstract: This paper presents for the first time a detailed study on information content of X-band single-pass interferometric spaceborne SAR data with respect to snow facies characterization. An approach for classifying different snow facies of the Greenland Ice Sheet by exploiting X-band TanDEM-X interferometric synthetic aperture radar acquisitions is firstly detailed. Large-scale mosaics of radar backscatter and volume correlation factor, derived from quicklook images of the interferometric coherence, represent the starting point for applying an unsupervised classification method based on the *c*-means fuzzy clustering algorithm. The data was acquired during winter 2010/2011. A partition of four different snow facies was chosen and interpreted using reference melt data, snow density, and in situ measurements. The variations in the stratification and micro-structure of firn, such as the variations of density with depth and the presence of percolation features, are identified as relevant parameters for explaining the significant differences in the observed interferometric signatures among different snow facies. Moreover, a statistical analysis of backscatter and volume correlation factor provided useful parameters for characterizing the snow facies behavior and analyzing their dependency on the acquisition geometry. Finally, knowing the location and characterization of the different snow facies, the two-way X-band penetration depth over the whole Ice Sheet was estimated. The obtained mean values vary from 2.3 m for the outer snow facies up to 4.18 m for the inner one. The presented approach represents a starting point for a long-term monitoring of ice sheet dynamics, by acquiring time-series, and is of high relevance for the design of future SAR missions as well.

Keywords: TanDEM-X; SAR; interferometric coherence; volume decorrelation; Greenland; Ice Sheet; snow facies

1. Introduction

The Greenland Ice Sheet, extending for about 1,700,000 km² over 80% of the entire Greenland surface, represents the second largest ice body on the planet after the Antarctic Ice Sheet. Its properties are significantly affected by temperature changes. Their knowledge can substantially contribute to a better understanding of the arctic and its response to climate change. Melt phenomena have strongly increased in the last years, therefore leading to modifications in the characteristics of the snow pack [1].

Previous studies of the Greenland Ice Sheet led to the definition of different snow facies, depending on the amount of snow melt and on the properties of the snow coverage itself. Using a large number of survey sites, C. S. Benson [2] divided the Ice Sheet into four zones, according to Figure 1. Melt does

not occur in the dry snow zone, which is situated at the highest altitudes at the center of the Greenland plateau. The snow is gradually compacted under its own weight and the surface layer is subject to modifications due to wind effects. Moreover, the properties of the dry snow zone are not uniform, since it is characterized by different levels of snow accumulations, systematically decreasing from the southwest to the northeast regions of Greenland [3,4]. This inner region is surrounded by the percolation zone, where a limited amount of melt per year occurs, leading to the generation of larger snow grains and to the formation of small ice structures, like lenses and pipes, within the snow pack. The size of such ice formations can vary from some centimeters to tens of centimeters [5]. The wet snow zone is located further down slope towards Greenland's coasts, where a substantial part of the snow melt drains off during summer, and is characterized by the presence of multiple ice layers. Outer coastal regions are finally classified as ablation zone, where the previous year accumulation completely melts during summer, resulting in a surface of bare ice and surface moraine. Up to now, the different facies have been located using microwave sensors by estimating the backscatter levels of the reflected signal [6,7]. The dry snow zone is characterized by low levels of backscatter, given the absorption of the incident radar wave; on the other hand, the presence of ice pipes and lenses in the percolation snow, whose dimensions are comparable to the wavelength of the incident radar wave, strongly increase the backscattered signal from such a region. The scattering mechanisms occurring in the wet snow zone are similar to those in the percolation zone, even though a higher variability is expected during summer, due to increased melt rates [5]. Moreover, the availability of several spaceborne SAR missions allows for the monitoring of radar backscatter evolution in time, demonstrating the great potential of radar to track down changes in the Ice Sheet properties [8].

The penetration of an incident radar wave on a snow pack is dependent on the sensor's frequency and wave polarization, and on the characteristics of the illuminated target, such as snow density and structure, leading to volume scattering. Interferometric synthetic aperture radar (SAR) acquisitions over the Greenland Ice Sheet are therefore subjected to volume decorrelation [9]. Its amount can be associated to the dominant backscattering mechanism for radar waves incident onto a snow pack, helping to classify the characteristics and structure of the snow pack itself.

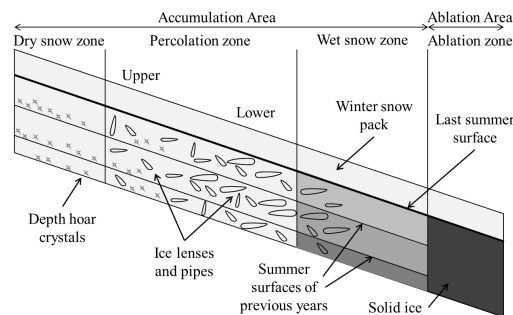


Figure 1. Greenland Ice Sheet facies, classified after C. S. Benson in [2]: the dry snow zone, where no melt occurs, the percolation zone, where a limited amount of melt per year occurs and meltwater percolates and then refreezes within the snow pack, the wet snow zone, where a substantial part of the snow melt drains off during summer, and the ablation zone, where the previous year accumulation completely melts during summer.

The German SAR mission TanDEM-X has the primary goal of generating a global, high-precision digital elevation model (DEM) with a spatial resolution of 12 m [10–12]. Since October 2010, two twin satellites TerraSAR-X and TanDEM-X have been flying in a close orbit configuration, acting as an X-band single-pass SAR interferometer and systematically scanning the Earth's land masses in bistatic single horizontal polarization stripmap mode, with a swath width of about 30 km. In this paper we present an approach to locate and investigate different snow facies by exploiting TanDEM-X

interferometric SAR acquisitions over the snow-covered areas of Greenland. TanDEM-X data, acquired in X-band at 9.6 GHz, are particularly suitable for this analysis due to the single-pass bistatic capabilities of the system, which does not suffer from temporal decorrelation [13]. As far as spaceborne SAR sensors are concerned, this data set is unique.

The goal of classification techniques is to group together the input data in different classes on the basis of a defined measure of similarity. The approach can either be supervised, if a priori knowledge is introduced for defining the properties of the different classes, or unsupervised, if such classes are directly estimated from the input data, without external additional information. Since only a few local studies have been performed for determining the properties of the Greenland and Antarctica Ice Sheets using X-band SAR data [14–16], only a limited a priori knowledge is available for directly defining the characteristics of each snow facies from X-band signatures. Unsupervised classification techniques, such as fuzzy clustering, therefore represent an attractive technique.

A first preliminary study on the potential of TanDEM-X interferometric data for snow facies analysis using fuzzy clustering was presented in [17]. We refined the classification algorithm, investigated its performance in detail, and performed comparisons with in situ observations to support interpretation of the results. In Section 3 we describe the large-scale mosaics of SAR backscatter and volume correlation factor, together with additional parameters, derived from systematic TanDEM-X interferometric acquisitions. These mosaics are the starting point for applying the *c*-means fuzzy clustering algorithm, detailed in Section 2.1. We present the obtained results in Section 4, where we also address the use of different number of clusters. Their interpretation is discussed in Section 5, by means of reference melt data, snow density, and in situ measurements of snow structure. A dedicated sub-clustering of the inner snow facies allows to further refine its classification, as discussed in Section 5.3. In Section 5.4, we present a statistical analysis of backscatter and volume decorrelation for the derived snow facies, which allows to fit a Gaussian model to the histograms of these quantities. Finally, knowing the location of the different facies, it is possible to estimate the X-band penetration depth along the whole Ice Sheet, as explained in Section 6, and to compare it to an independent estimation, obtained by composing TanDEM-X digital elevation model (DEM) data and ICESat laser altimeter measurements. Conclusions are finally drawn in Section 7.

2. Fuzzy Clustering for Snow Facies Classification

In this section we describe the method used to classify the different snow facies of the Greenland Ice Sheet. It is based on the use of the *c*-means fuzzy clustering algorithm, developed by J. Bezdek et al. in [18], which is an unsupervised classification algorithm based on fuzzy logic theory.

In this work, two characterizing radar quantities are considered for classifying snow facies: radar backscatter and coherence contribution due to volume decorrelation. The choice of an unsupervised classification method resides in the fact that a gradual transition of backscattering intensity between different snow facies on the Greenland Ice Sheet was observed by K. C. Partington in [19], impairing the use of a manual partitioning approach, which would strongly depend on the subjective choice of the decision thresholds. Moreover, the *c*-means fuzzy clustering algorithm has already been used in the literature for discriminating snow facies using Envisat active and passive microwave observations, showing it to be a promising approach for clustering similar regions of the Greenland Ice Sheet, as presented by Tran et al. in [20].

2.1. The Fuzzy *c*-Means Clustering Optimization

Clustering defines the task of grouping together elements coming from an input set of observations, depending on how similar they are to each other. The observations are divided into *c* non-empty subsets called clusters. Since in reality clusters may show some kind of overlap, fuzzy-clustering has been introduced [21]. The fuzzy *c*-means clustering algorithm is an iterative optimization algorithm which allows the determination of the optimal cluster centers without requiring a priori information [22]. In literature, the fuzzy *c*-means clustering has been found to be very popular

within the research community, being used for a large variety of applications, such as risk and claim classification or vehicular pollution estimation [23,24].

The idea is to represent the similarity that an observation shares with each cluster by using a membership function, whose values are between 0 (0% probability of belonging to cluster i) and 1 (100% probability of belonging to cluster i). The results are fuzzy c -partitions of the input observation data set, which contain observations characterized by a high intracluster similarity and a low extracluster one.

For a given input vector of N observations, defined as $\mathbf{Y} = [\mathbf{y}_k]$ ($k = 1, \dots, N$), where each \mathbf{y}_k is characterized by P features, the membership function can be expressed using a $c \times N$ real matrix $\mathbf{U} = [u_{ik}]$. The i^{th} cluster center is then identified by a P -dimensional tie-point vector \mathbf{v}_i .

If cluster centers are not known by *a priori* considerations, an optimization method has to be applied in order to estimate them. Their locations are iteratively determined by optimizing the following objective function:

$$J = \sum_{i=1}^c \sum_{k=1}^N (u_{ik})^m \|\mathbf{y}_k - \mathbf{v}_i\|^2 \quad (1)$$

where $d_{ik}^2 = \|\mathbf{y}_k - \mathbf{v}_i\|^2$ is the squared Euclidean distance from point \mathbf{y}_k to the cluster center \mathbf{v}_i . The parameter m controls the fuzziness of the algorithm: $m = 1$ produces hard partitions of \mathbf{Y} , while increasing m allows the single clusters to overlap, blurring the membership degree to higher levels of fuzziness. Since the Euclidean distances of the observations from the cluster centers in Equation (1) have to be minimized, it is important to scale the different features to the same order of magnitude, in order to avoid having a predominant one, which would affect the classification accuracy. In this work, we decided to normalize each input set of features to a unit standard deviation as:

$$\hat{\mathbf{Y}}_p = \mathbf{Y}_p / \sigma_p \quad (2)$$

where \mathbf{Y}_p is a vector containing the N input values of \mathbf{Y} for the p^{th} feature and σ_p is the standard deviation.

By substituting the normalized input data set $\hat{\mathbf{Y}} = [\hat{\mathbf{y}}_k]$ into (1), the optimal clustering of $\hat{\mathbf{Y}}$ is therefore obtained as:

$$(\hat{\mathbf{U}}, \hat{\mathbf{v}}) = \arg \min_{\mathbf{U}, \mathbf{v}} (J) \quad (3)$$

$\hat{\mathbf{U}}$ and $\hat{\mathbf{v}}$ can be optimized by iterating over the following equations:

$$\hat{\mathbf{v}}_i = \frac{\sum_{k=1}^N (\hat{u}_{ik})^m \mathbf{y}_k}{\sum_{k=1}^N (\hat{u}_{ik})^m}, \quad 1 \leq i \leq c \quad (4)$$

$$\hat{u}_{ik} = \left(\sum_{j=1}^c \left(\frac{\hat{d}_{ik}}{\hat{d}_{jk}} \right)^{\frac{2}{m-1}} \right)^{-1}, \quad 1 \leq k \leq N, 1 \leq i \leq c \quad (5)$$

After a random initialization of $\hat{\mathbf{U}}$, (4) and (5) are iteratively updated until convergence is obtained. A convergence test can be performed by computing the mean square error between $\hat{\mathbf{U}}$ at steps α and $\alpha + 1$.

A recurrent issue of the c -means clustering algorithm is to remain stuck in a local minimum, being unable to provide a meaningful set of cluster centers. A proper initialization of the cluster centers is therefore highly recommended, as presented in the next section.

2.2. Algorithm Initialization

The algorithm initialization represents a crucial step in avoiding local minima. Many investigations have been carried out on finding an effective initialization for the algorithm; in this paper we based

our initialization on the work presented in [25]. The input set of normalized observations per feature \hat{Y}_p is transformed into a positive vector \tilde{Y}_p by:

$$\tilde{Y}_p = \hat{Y}_p - \min(\hat{Y}_p) \quad (6)$$

Now the Euclidean distances of each scaled observation from the origin are evaluated and sorted in increasing order. The corresponding scaled observations are sorted accordingly. Given the desired number of output clusters c , the sorted observations are grouped together into c subsequent sub-sets, each of those composed of N/c observations. For each sub-set, a cluster center is then initialized by evaluating, for each feature, the mean value of all available observations.

3. Input Data: TanDEM-X Mosaics over Greenland

In this section, we present the input data set of TanDEM-X interferometric acquisitions used for classifying Greenland Ice Sheet snow facies, together with the derivation of a mask of ice/no-ice covered regions to which our analysis has been confined.

3.1. TanDEM-X Acquisitions over Greenland

The Greenland Ice Sheet has been almost completely covered with TanDEM-X for the first time during winter 2010–2011, when the snow conditions are assumed to be stable, since melt does not significantly occur. All these interferometric SAR acquisitions have been used for the present investigation.

For processing reasons, TanDEM-X acquisitions are then split into ground scenes with an extension of about 30 km in range and 50 km in azimuth.

For each scene, the operational TanDEM-X processor delivers several quicklook images as by-products from the interferometric processing chain [26]. These quicklooks are characterized by a lower resolution compared to the corresponding interferometric data at full resolution, having a ground pixel spacing of about 50 m \times 50 m, and are generated for several different quantities, such as the amplitude, the interferometric coherence, and the resulting DEM.

3.2. TanDEM-X Input Mosaics

The new approach for classifying different snow facies of the Greenland Ice Sheet consists of exploiting the information coming from both the radar backscatter and the volume decorrelation, derived from the interferometric coherence. Large-scale mosaics of such quantities can be generated by composing quicklook images together, with the constraint of selecting an output resolution equal or larger than the one of each single input image [27,28]. For the current work the selected pixel spacing is $0.002^\circ \times 0.006^\circ$ in latitude/longitude coordinates, which, at a latitude of 73° N and longitude of 40° W, at the center of Greenland, corresponds to a ground resolution of about 200 m \times 200 m.

A mosaic of γ^0 , the backscatter level projected in the plane perpendicular to the slant range direction, is depicted in Figure 2a. This projection has been chosen because, with respect to the other projections in the slant range plane (β^0) or on ground (σ^0), it is the one which, for an homogeneous type of backscatter, shows a relatively constant reflectivity over a wide range of incidence angles [29].

The coherence contribution due to volume decorrelation can be estimated from the total interferometric coherence as explained as follows. The total interferometric coherence can be decomposed into different correlation factors [10]:

$$\gamma_{\text{Tot}} = \gamma_{\text{SNR}} \gamma_{\text{Quant}} \gamma_{\text{Amb}} \gamma_{\text{Rg}} \gamma_{\text{Az}} \gamma_{\text{Vol}} \gamma_{\text{Temp}} \quad (7)$$

where the different terms on the right-hand side of (7) identify the contributions due to limited signal-to-noise ratio (SNR) (γ_{SNR}), quantization (γ_{Quant}), ambiguities (γ_{Amb}), baseline decorrelation (γ_{Rg}), relative shift of the Doppler spectra (γ_{Az}), volume decorrelation (γ_{Vol}), and temporal

decorrelation (γ_{Temp}). Since the total coherence decomposition proposed in (7) is a multiplicative model, it has to be clarified that the higher each single correlation factor is, the higher the resulting total coherence will be. The volume correlation factor γ_{Vol} is inversely proportional to the amount of volume decorrelation occurring in the data and represents the quantity that, from now on, we take into account for quantifying the impact of volume decorrelation on the total coherence.

As explained in Section 1, the volume correlation factor γ_{Vol} is a good indicator of snow characteristics. This contribution must therefore be isolated from the total interferometric coherence, which is available for each TanDEM-X interferometric acquisition. γ_{Vol} can be derived from (7) as:

$$\gamma_{Vol} = \frac{\gamma_{Tot}}{\gamma_{SNR} \gamma_{Quant} \gamma_{Amb} \gamma_{Rg} \gamma_{Az} \gamma_{Temp}} \quad (8)$$

In the specific case of TanDEM-X:

- $\gamma_{SNR} = 1/(1 + SNR^{-1})$, where SNR is the signal-to-noise ratio and is assumed to be equal in both monostatic and bistatic images:

$$SNR = \frac{\beta^0 \sin \theta - NESZ}{NESZ} \quad (9)$$

being β^0 the radar brightness, θ the local incidence angle, and NESZ the noise equivalent sigma zero. For the different operational TanDEM-X beams, the NESZ profiles used are depicted in Figure 3a, which have been evaluated as in [10].

- γ_{Quant} is computed by interpolating the look-up-table functions in Figure 3b, derived from real TanDEM-X data [30]. Block adaptive quantization (BAQ) has been used [31].
- According to the performance estimation analysis for TanDEM-X [10], γ_{Amb} , γ_{Rg} , and γ_{Az} are assumed to introduce a further overall correlation factor of 0.98 (2%).
- $\gamma_{Temp} \simeq 1$, since images are acquired in bistatic configuration.

The resulting mosaic of γ_{Vol} is shown in Figure 2b. It can be seen that, even though the illuminated area on ground is homogeneous, a slight dependency of γ_{Vol} on the slant range for each scene remains, showing a higher γ_{Vol} at the beam's borders (near and far range). This is due to the fact the estimated γ_{SNR} was computed by using theoretical NESZ profiles, due to a not perfect compensation of the range antenna pattern.

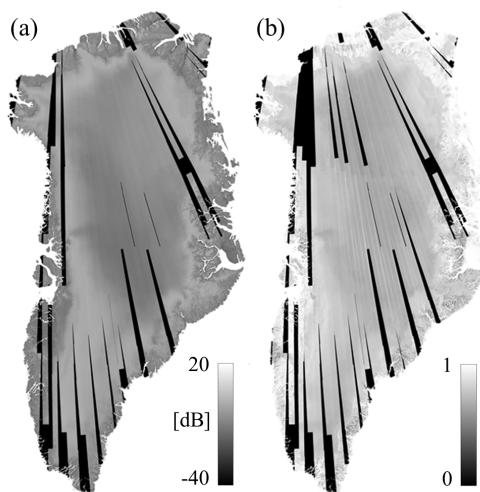


Figure 2. (a) Mosaic of the backscatter γ^0 over Greenland with a resolution of $200 \text{ m} \times 200 \text{ m}$. (b) Corresponding mosaic of the volume correlation factor γ_{Vol} . The composed TanDEM-X acquisitions were acquired in winter 2010–2011. Areas where no data are available are depicted in black.

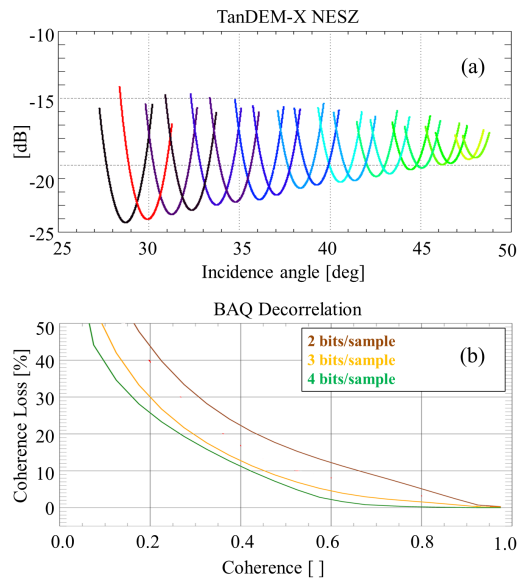


Figure 3. (a) NESZ (Noise Equivalent Sigma Zero) profiles for the operational TanDEM-X beams [10]. (b) Coherence loss due to BAQ (Block Adaptive Quantization). Each curve identifies a different quantization rate (2, 3, and 4 bits/sample).

3.3. Generation of the Ice Sheet Mask

The main part of the Greenland Ice Sheet is flat and is surrounded by mountainous regions characterized by rough topography. Therefore, more gradual variations of both backscatter and topography are expected over the Ice Sheet, with respect to the outer regions. In order to discriminate the Ice Sheet from ice-free areas, a mask is generated by setting thresholds on the local variance of both backscatter and local terrain slope.

The starting point to generate a map of local slope is the DEM quicklook image $D(x, y)$, generated for each TanDEM-X interferometric scene by the operational TanDEM-X processor. x and y are the longitude and latitude dimensions, respectively, converted into spatial distances. A slope map can be generated by evaluating the local DEM gradient $\nabla D(x, y)$, which can be decomposed into the horizontal and vertical components as:

$$\nabla D(x, y) = \left(\frac{\partial D(x, y)}{\partial x}, \frac{\partial D(x, y)}{\partial y} \right) \quad (10)$$

Then, the predominant local slope $\Lambda(x, y)$ is retrieved by computing the Euclidean norm of the gradient vector:

$$\Lambda(x, y) = \sqrt{\left(\frac{\partial D(x, y)}{\partial x} \right)^2 + \left(\frac{\partial D(x, y)}{\partial y} \right)^2} \quad (11)$$

For each γ^0 pixel (in dB unit), its local variance $\sigma_{\gamma^0}^2$ has been evaluated as:

$$\sigma_{\gamma^0}^2 = E[(\gamma^0)^2] - (E[\gamma^0])^2 \quad (12)$$

by computing the mean value $E[\cdot]$ on a window of 5×5 pixels around the center one. The local variance of the slope map σ_{Λ}^2 has been evaluated following the same approach. Two thresholds have been empirically set at $\sigma_{\gamma^0}^2 = 1$ dB and $\sigma_{\Lambda}^2 = 2\%$. The slope map of Greenland and the corresponding permanent ice mask are depicted in Figure 4a,b, respectively. Note that the border samples of missing acquisitions are filtered out as well, since the local variance between real data and missing ones within the γ^0 mosaic is obviously high (see Figure 2a).

The obtained Ice Sheet mask has been verified by comparing it to the PROMICE (Programme for Monitoring of the Greenland Ice Sheet) aerophotogrammetric map of Greenland ice masses over different test sites [32]. An example is presented in Figure 5, where the two test sites identified by the red rectangles in Figure 4b are considered. Good results are obtained over the Ice Sheet, while the method frequently fails on outlet glaciers due to the presence of crevasses, small scale features, and steep topography. Nevertheless, since we are focusing our attention on the whole Ice Sheet and not on its borders, we assume the derived Ice Sheet mask to be accurate enough for our purposes. The areas classified to be permanent ice- and snow-covered regions within the TanDEM-X mask are finally taken into account as input observations for locating the different snow facies of the Greenland Ice Sheet.

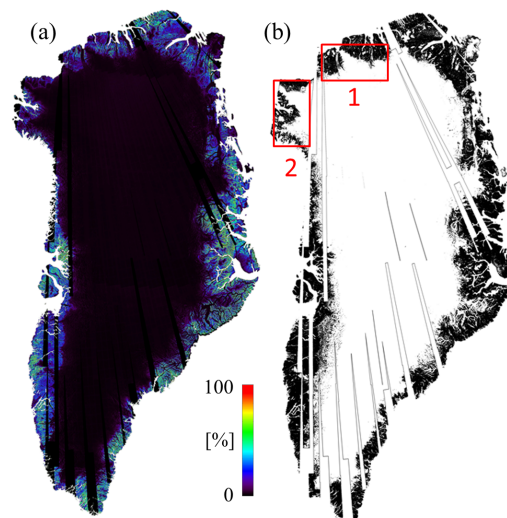


Figure 4. (a) Slope map over Greenland derived from TanDEM-X digital elevation data. (b) Mask of permanent ice areas. White corresponds to the Ice Sheet and black to ice-free areas, derived from the local variance of TanDEM-X backscatter and terrain slope. The red squares identify two test sites used for verification, as presented in Figure 5.

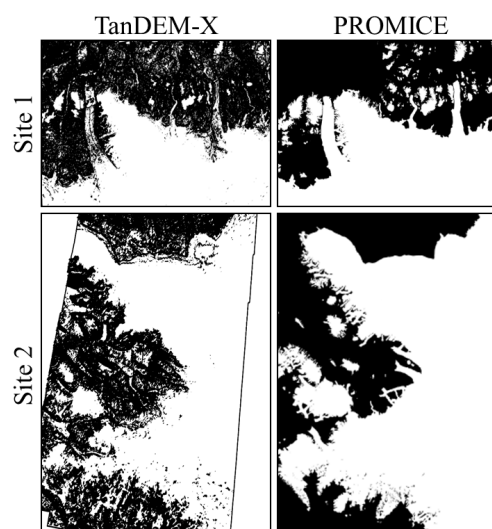


Figure 5. Comparison between masks of permanent ice- and snow-covered regions of Greenland, derived from TanDEM-X interferometric data, and the PROMICE aerophotogrammetric map of Greenland ice masses [32].

4. Classification Results

In this section we present the results obtained by applying the classification method, described in Section 2, to the input data set of interferometric TanDEM-X acquisitions, presented in Section 3. We selected $P = 2$ features, namely γ^0 and γ_{Vol} , and tested different numbers of clusters. We report here the results obtained using $c = 3, 4, 5$ number of clusters. The m parameter was set to 2. The resulting membership maps are displayed in Figure 6. A high percentage corresponds to a high probability of belonging to a specific cluster. The classification results for the three different sets of clusters are presented in Figure 7a–c. The corresponding normalized histograms of the input data, together with the location of the cluster centers \hat{v} , are depicted in Figure 7d–f, where the horizontal and vertical axis display the normalized volume correlation factor $\tilde{\gamma}_{\text{Vol}}$ and the normalized backscatter $\tilde{\gamma}^0$, evaluated as:

$$\tilde{\gamma}_{\text{Vol}} = \frac{\gamma_{\text{Vol}}}{\sigma_{\gamma_{\text{Vol}}}} - \min\left(\frac{\gamma_{\text{Vol}}}{\sigma_{\gamma_{\text{Vol}}}}\right) \quad (13)$$

$$\tilde{\gamma}^0 = \frac{\gamma^0}{\sigma_{\gamma^0}} - \min\left(\frac{\gamma^0}{\sigma_{\gamma^0}}\right) \quad (14)$$

being $\sigma_{\gamma_{\text{Vol}}}$ and σ_{γ^0} the standard deviations of γ_{Vol} and γ^0 , respectively. For the considered input data set, we have $\min(\gamma_{\text{Vol}}) = 0.14$, $\sigma_{\gamma_{\text{Vol}}} = 0.08$, $\min(\gamma^0) = -24.7$ dB, and $\sigma_{\gamma^0} = 3.94$ dB. The cluster centers for the selected partition in the normalized histogram of the input data are given in Figure 8.

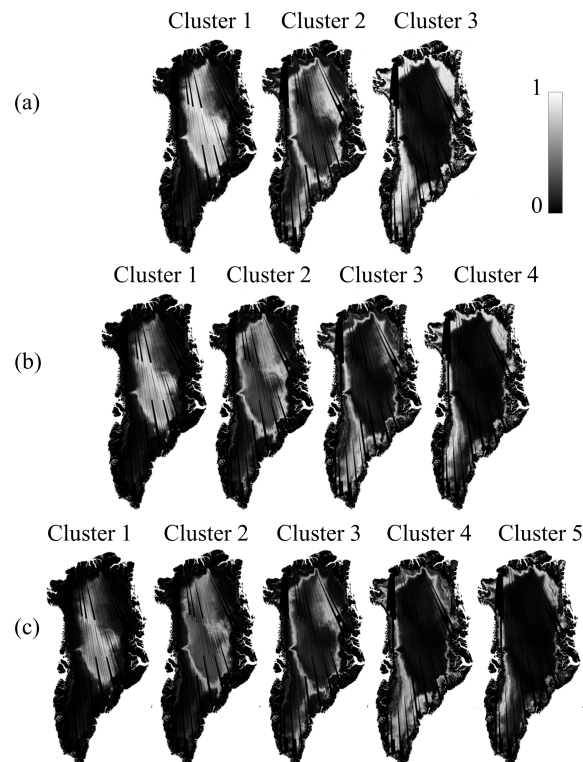


Figure 6. Membership values for each pixel belonging to the Ice Sheet, for the different set of cluster centers used for classifying the Greenland Ice Sheet. (a) three clusters, (b) four clusters, (c) five clusters.

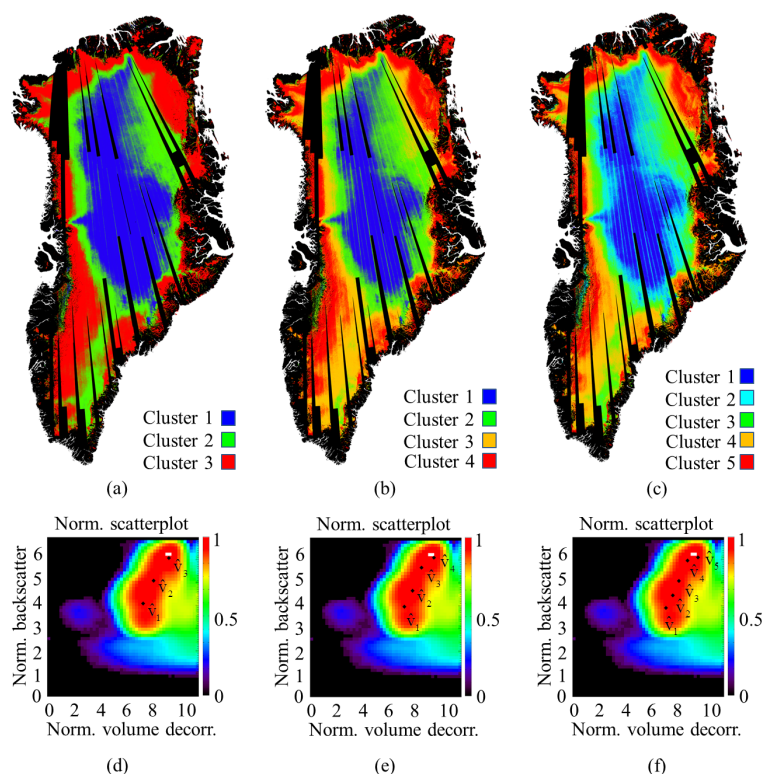


Figure 7. Classification of the Greenland Ice Sheet facies using (a) three, (b) four, and (c) five clusters; together with the corresponding normalized histograms of the input data and the locations of the cluster centers \hat{v} (d–f). The white rectangles locate the maximum of the histogram.

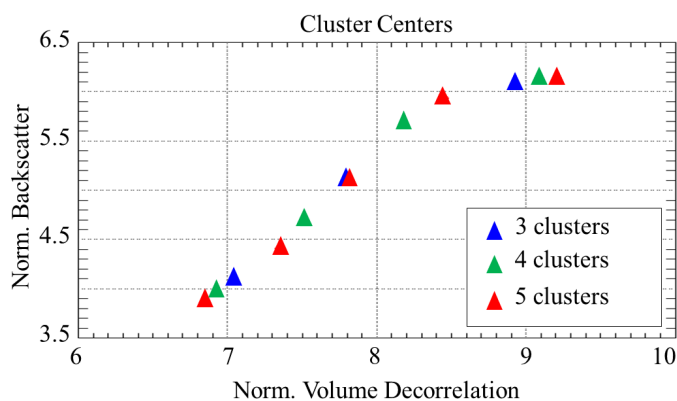


Figure 8. Location of cluster centers in the normalized input domain.

The fuzzy partition of three clusters shows a higher distance among the single cluster centers. Higher numbers of clusters are also characterized by a higher degree of inter-cluster overlap and result in a classification where lower values of the membership matrix \hat{U} are accepted for associating a certain cluster to an input observation. Nevertheless, increasing the number of clusters allows to get a more detailed characterization of the different snow facies, strongly influenced by increasing melt phenomena from the center of the plateau toward the outer edges.

The algorithm was run using a higher a-priori number of clusters c as well, obtaining partitions characterized by a very limited extend and increasing the confusion between adjacent classes. Such a trend is already visible when using $c = 5$ (Figure 7c), where cluster 2 (light blue) corresponds to a very thin intermediate layer between cluster 1 (blue) and cluster 3 (green) and is entirely characterized

by the presence of pixels classified as both cluster 1 and 3. This trend is maintained for higher number of cluster centers and the results are here omitted.

Furthermore, for the three different numbers of selected clusters presented in Figure 7, the percentage of pixels classified accordingly to a membership value which is higher than 0.3, 0.5, 0.7 and 0.9 are summarized in Table 1. The results indicate that, using four clusters, over 81% of the pixels are classified with a membership value above 0.5. From a pure algorithmic point of view, such a partition shows therefore a reasonably good performance in terms of classification reliability.

Table 1. Percentage of pixels for each set of clusters classified according to a membership value \hat{u}_{ik} higher than 0.9, 0.7, 0.5, and 0.3.

Clusters	$\hat{u}_{ik} > 0.9$ (%)	$\hat{u}_{ik} > 0.7$ (%)	$\hat{u}_{ik} > 0.5$ (%)	$\hat{u}_{ik} > 0.3$ (%)
3	23.8	64.2	91.3	100.0
4	12.7	46.8	81.2	98.9
5	8.9	35.4	69.0	96.8

Based on this finding, we decided to consider the partition with $c = 4$ for our further investigation, which represents a good trade-off between a satisfying level of detail and a good separation between adjacent clusters. From now on, we will therefore refer to snow facies instead of clusters and we will consider the map presented in Figure 7b as reference, characterized by the presence of 4 different snow facies.

Finally, by considering an overall Ice Sheet surface of 1,700,000 km², it is possible to estimate the extension of each snow facies. The results are presented in Table 2.

Table 2. Extension of the four Ice Sheet snow facies derived with TanDEM-X data, with respect to the overall Ice Sheet surface of 1,700,000 km², in % and in km².

Facies	Ice Sheet Percentage (%)	Extension (km ²)
Facies 1	24.1	409,700
Facies 2	27.8	472,600
Facies 3	21.9	372,300
Facies 4	26.2	445,400

5. Snow Facies Interpretation and Further Considerations

The interpretation of the derived snow facies map represents a challenging task, since no global reference data, derived from interferometric SAR acquisitions, is available for a direct comparison. To better understand the properties of each derived snow facies we used reference melt data, derived from passive microwave sensors, and in situ measurements (Sections 5.1 and 5.2). This approach allows us to characterize the derived snow facies by comparing them to physical parameters such as average amount of snow melt per year, snow density, and structure. Further considerations on the inner snow facies, characterizing statistical parameters, and volume decorrelation dependency on the height of ambiguity are then addressed in Sections 5.3–5.5. A summary of the considerations expressed in this section is finally given in Section 7.

5.1. Reference Snow Melt Data

As reference melt data we considered the map presented in Figure 9b, derived from spaceborne passive microwave sensors as presented by M. Tedesco in [33]. It shows the average amount of melt days per year during the time span between 1981 and 2010, at a resolution of 25 km × 25 km. Such a long time span has been taken into account in order to be able to identify the dry snow zone, where no significant melt has occurred for at least several years before the observations were carried out.

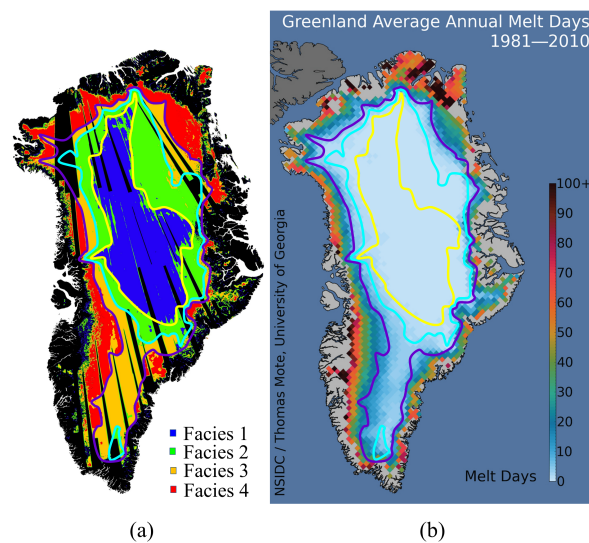


Figure 9. (a) Estimated snow facies of the Greenland Ice Sheet from TanDEM-X data with a ground resolution of about $4 \text{ km} \times 4 \text{ km}$. The contour lines identify the borders between facies 1 and 2 (yellow), facies 2 and 3 (light blue), and facies 3 and 4 (violet), respectively. (b) Average melt days per year from 1981 to 2010, derived from passive microwave sensors [33].

It is well known that a melt anomaly occurred in summer 2012, characterized by the presence of melt events across almost the entire Ice Sheet. This caused melt/freeze metamorphism with a consequent increase of backscatter levels also over the Greenland dry snow zone [34]. This fact resulted in reduced penetration for CryoSat [35] and possibly also for TanDEM-X. It is therefore important to notice that the data used for the current investigation were acquired before such events, after a quite stable period of several years, documented by the collection of data provided by the C-band scatterometer ASCAT from 2007 onwards [36].

To perform the comparison, we then derived the borders between different snow facies of the TanDEM-X classification map. To do so, we first low-pass filtered the classification map in Figure 7b using a two-dimensional Gaussian low-pass filter with passband bandwidth at -3 dB equal to 5% of the total bandwidth, obtaining a map with resolution of about $4 \text{ km} \times 4 \text{ km}$ on ground, and then re-quantized it to the 4 available cluster values by applying nearest-neighbor interpolation. The obtained results are shown in Figure 9a. At this point, we manually derived three polygons by visual inspection, by selecting tie-points at the border between two adjacent classes (Figure 9a): between the snow facies 1 and 2 (yellow), 2 and 3 (light blue), and 3 and 4 (violet), respectively. The same polygons have also been superimposed onto the melt data in Figure 9b.

Facies 1 is mostly unaffected by snow melt. Facies 2 is confined between only a few days and less than ten days of melt per year, while facies 3 is located where melt starts to be considerable (between about ten and twenty days per year). Finally, facies 4 is mostly characterized by more than 20 days of melt per year. The first consideration that can be drawn from this analysis is that facies 1 is principally characterized by the presence of permanently dry snow while the other snow facies belong to a transition zone with increasing melt phenomena toward the outer regions of the Ice Sheet.

5.2. In Situ Measurements along the EGIG Line

Up to now, many scientific expeditions have been carried out in Greenland to empirically collect data on the state of the Ice Sheet. In particular, several of those acquired data along sections of the Expédition Glaciologique Internationale au Groenland (EGIG) line, a traverse route across the plateau at about 70° N [37]. In the last years, selected test sites along the EGIG line were used for supporting the

CryoSat Mission [38] with in situ measurements. Some of those are presented in Figure 10, where test sites from T03 to T43 are superimposed on the derived snow facies map.

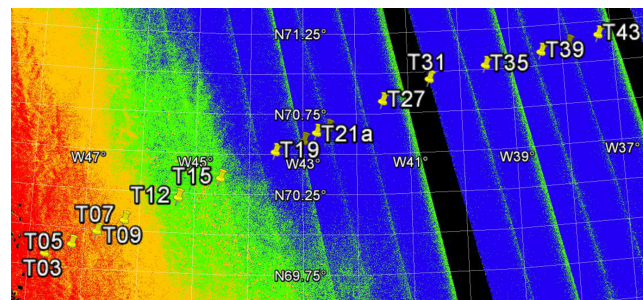


Figure 10. Test sites along the EGIG line used for supporting the CryoSat mission with in situ measurements, superimposed on the snow facies map as derived in Figure 7b. (Data overlaid in ©Google Earth).

Scott et al. in [39] analyzed the spatial variation of snow density with depth from in situ measurements at T03, T05, T07, and T12, performed in spring and autumn 2004 and spring 2006. They report that:

- T03 (belonging to facies 4) shows the presence of percolation features, such as ice layers and lenses, generated by meltwater and positioned under the summer melt level.
- at T05 (situated at the transition between facies 3 and facies 4), percolation features do not always reach the melt surface of the previous summer. Moreover, because of percolation, an additional moderate densification was observed beneath the previous upper end of summer surface, suggesting that most of the percolating water refreezes before reaching the previous summer surface.
- Between T07 and T12 (situated approximately at the outer and inner borders of facies 3) the depth at which percolation features could be found significantly decreased.

Morris and Wingham reported snow density measurements from T05 to T41 in [40], obtained using the neutron probe during field campaigns from 2004 to 2006. From their work, we can assess that:

- T05 is situated in the percolation zone and characterized by the considerable presence of thick ice layers within the snow pack.
- A transition zone has then been detected between T05 and T21, which matches the borders of the dry snow zone.
- T21 (belonging to facies 1) is indicated as the start of the dry snow zone. From our analysis, the assigned snow facies 1 appears in that region to be slightly more extended toward the outer Ice Sheet of about 30 km.
- Significant differences in the vertical structure are detectable between T12 and T21 (Figure 5 in [40]), being high-density melt layers clearly visible at T12 only.
- Mean snow density, accumulation rate, and mean snow temperature decrease almost gradually along the EGIG line (from outer to inner regions).

These observations suggest that changes in mean snow density are not suitable for explaining the significant differences in the observed signatures of backscatter and volume correlation factor among the estimated facies, since variations of the mean snow density are small. More relevant are the variations in the stratification and micro-structure of firn, such as the variations of density with depth and the presence of percolation features. As presented by Scott et al. in [41], ice inclusions in the percolation zone produce a complex radar return, characterized by the superposition of multiple strong reflectors within a volume, impacting the characteristic interferometric signature of the acquired radar signal. From the distributions of both backscatter and volume correlation factor from each estimated

facies, it is seen how, within the transition zone, outer facies 3 and 4, where a significant presence of percolation features is detected (e.g., at T03 and T05), are characterized by higher values of both backscatter and volume correlation factor. Facies 2, on the contrary, is characterized by lower values of both quantities, probably related to the decrease of percolation features within the snow pack.

5.3. Refined Classification of the Inner Snow Facies

Based on the considerations drawn in Section 5.1, we can assume the derived inner snow facies (facies 1) to be dominated by the presence of dry snow. Even if melt does not occur within the whole dry snow zone, this snow facies is characterized by the presence of different types of snow. This can be explained by the lower snow accumulation rate and larger grain size in the north-east part of Greenland [3,42]. Such differences cannot be so clearly detected by γ_{Vol} , but are well visible if γ^0 is considered. This becomes clear when looking at the mosaic of the SNR in Figure 11a, which is lower in the inner southern part of snow facies 1, resulting into a decrease of γ_{SNR} . Such loss in the total coherence is therefore compensated with the evaluation of γ_{Vol} . A refinement of the classification of facies 1 can be done by performing a sub-clustering, taking into account as input data pixels classified as dry snow zone. In this way, the algorithm is able to detect smaller differences than when applied to the whole Ice Sheet. The results using two sub-clusters are presented in Figure 11b, together with the membership matrix in Figure 11c, and the normalized histogram of the input data in Figure 11d. The following values were obtained from the input data for the computation of $\tilde{\gamma}_{Vol}$ and $\tilde{\gamma}^0$: $\min(\gamma_{Vol}) = 0.14$, $\sigma_{\gamma_{Vol}} = 0.04$, $\min(\gamma^0) = -24.7$ dB, and $\sigma_{\gamma^0} = 2.09$ dB. The two classes can be associated to a southern (light blue) and a northern (violet) sub-facies, characterized by higher and lower snow accumulation rates, respectively.

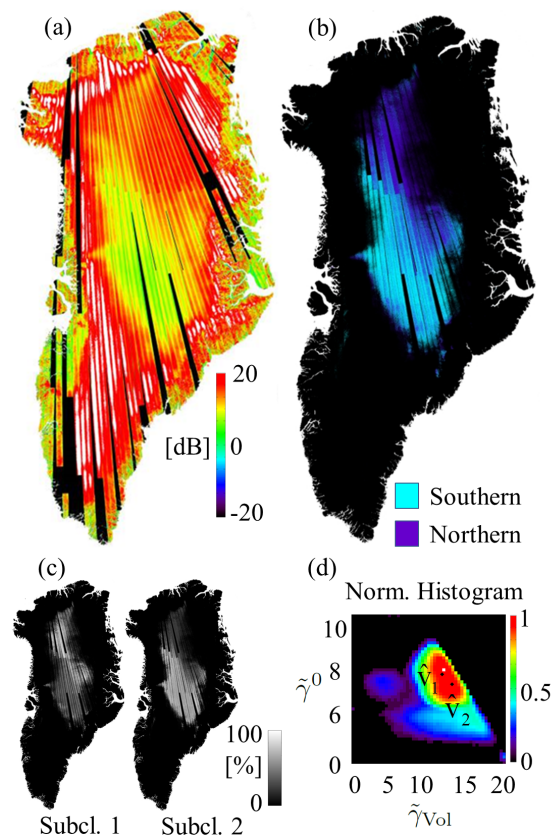


Figure 11. (a) Mosaic of the SNR for the considered TanDEM-X acquisitions. (b) Refined classification of facies 1 into a northern (violet) and a southern (light blue) sub-facies. (c) Membership values for each pixel for the two sub-clusters. (d) Histogram of the input data in the normalized domain.

5.4. Statistical Analysis of the Derived Snow Facies

We can now analyze the statistical properties of the derived snow facies in terms of backscatter γ^0 and volume correlation factor γ_{Vol} . To do so, we evaluated the histograms of these quantities for each snow facies separately, as presented in Figure 12 (filled red area). The histograms of backscatter γ^0 have been directly derived from γ^0 in dB. As it can be seen, each distribution can be clearly fitted by using a Gaussian function, except for γ^0 of facies 1, where two peaks are visible and a better fitting can be performed by summing two Gaussian distributions (Figure 12(a1)), as confirmed by the refined classification explained in Section 5.3. The variation of γ_{Vol} from the southern to the northern facies 1 is much less accentuated and a single Gaussian fitting has been used for the whole facies. Mean values and standard deviations, evaluated in linear scale, of γ^0 and γ_{Vol} for the different snow facies are presented in Table 3.

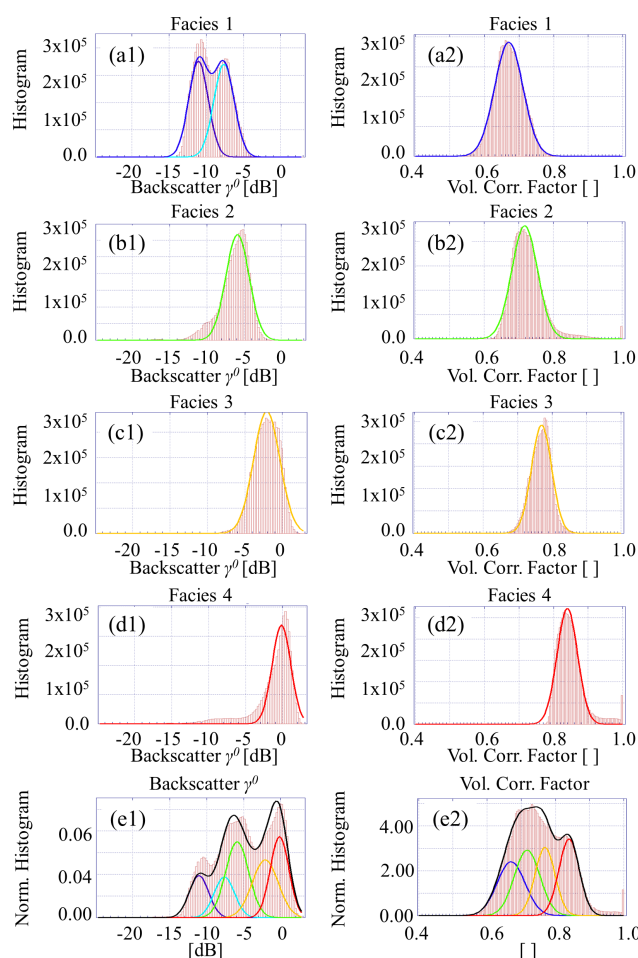


Figure 12. Histograms of the backscatter γ^0 and of the volume correlation factor γ_{Vol} (filled red area), and corresponding Gaussian fitting (solid curves) for facies 1 (a1,a2), facies 2 (b1,b2), facies 3 (c1,c2), and facies 4 (d1,d2). The sum of two Gaussian curves in plot (a1) has been used for fitting the γ^0 of inner snow facies (facies 1). (e1) Overall normalized histogram of the total backscatter γ^0 (red bars) and sum of the five fitting Gaussian distributions (black) derived for the different facies. (e2) overall normalized histogram of the total volume correlation factor (red bars) and sum of the four fitting Gaussians (black) derived for the different facies.

We can now use the fitted Gaussian distributions to characterize the overall distribution of γ^0 in dB and γ_{Vol} over the Greenland Ice Sheet as:

$$G(x) = \sum_{i=1}^{N_f} \frac{1}{\sqrt{2\pi\nu_{1,i}^2}} \exp\left(-\frac{(x - \nu_{2,i})^2}{2\nu_{3,i}^2}\right) \quad (15)$$

where N_f identifies the number of facies and x is either γ^0 ($N_f = 5$) or γ_{Vol} ($N_f = 4$). The estimated set of fitting coefficients ν is given in Table 4. The overall normalized histograms of both γ^0 and γ_{Vol} , together with the corresponding modeled Gaussian distributions, are shown in Figure 12(e1,e2).

Table 3. Mean values and standard deviations of γ^0 and γ_{Vol} for the different snow facies. γ^0 values are displayed in both linear and logarithmic scale.

Facies	Backscatter γ^0				Volume Correlation Factor γ_{Vol}	
	Mean		Std. Dev.		Mean	Std. Dev.
	()	(dB)	()	(dB)	()	()
1 (southern)	0.095	−10.21	0.033	−14.76	0.67	0.04
1 (northern)	0.172	−7.63	0.067	−11.73		
2	0.253	−5.96	0.101	−9.95	0.73	0.05
3	0.664	−1.78	0.247	−6.07	0.77	0.03
4	0.883	−0.54	0.365	−4.37	0.85	0.04

Table 4. Gaussian fitting coefficients for modeling the distributions of γ^0 and γ_{Vol} as in Equation (15).

Facies	Backscatter γ^0			Volume Correlation Factor γ_{Vol}		
	$\nu_{1,i}$	$\nu_{2,i}$	$\nu_{3,i}$	$\nu_{1,i}$	$\nu_{2,i}$	$\nu_{3,i}$
1 (southern)	0.127	−11.056	1.316			
1 (northern)	0.129	−7.620	1.373	0.247	0.670	0.041
2	0.274	−5.888	1.561	0.274	0.717	0.037
3	0.235	−2.087	1.761	0.223	0.769	0.029
4	0.235	−0.148	1.256	0.254	0.839	0.029

5.5. Volume Decorrelation Dependency on the Height of Ambiguity

In presence of volume scattering, the volume correlation factor γ_{Vol} is influenced by the acquisition geometry. The phenomena can be analyzed in terms of dependency of γ_{Vol} on the height of ambiguity h_{amb} , which corresponds to the height difference equivalent to a complete 2π phase cycle in the interferogram and, for a bistatic acquisition, is defined as [10]:

$$h_{\text{amb}} = \frac{\lambda r \sin \theta}{B_{\perp}} \quad (16)$$

where λ is the radar wavelength, r the slant range, θ the incidence angle, and B_{\perp} the normal baseline. Several investigations on this topic have been already performed within the TanDEM-X mission over forested areas, showing a significant increase of γ_{Vol} with h_{amb} [13].

Since such a dependency changes with the characteristics of the snow pack and the scattering mechanisms involved, it has not been possible to introduce a correction factor on γ_{Vol} before applying the c -means fuzzy clustering algorithm to mitigate such effects, being that the location of the different snow facies is unknown. Hence, a statistical analysis has been carried out afterwards for each estimated snow facies separately, aim to better investigate such a dependency. We grouped together the different h_{amb} per input acquisition in intervals of 0.5 m each, evaluating the corresponding distribution of γ_{Vol} . For each snow facies, we noticed that no significant trend is detectable, probably due to the fact that we are observing a limited span of heights of ambiguity. The clearest trend was observed over facies

3 and is presented in Figure 13. The plot shows the mean values and standard deviations of γ_{Vol} for the different height of ambiguity intervals (vertical axis on the left-hand side), while the number of input measurements in logarithmic scale for each interval of the height of ambiguity is depicted in blue (vertical axis on the right-hand side). Results obtained for $h_{amb} > 53$ m and $h_{amb} < 40$ m are to be considered unreliable, since only a few input measurements were available. An overall slight increase of γ_{Vol} of about 0.05 is visible.

Therefore, not introducing a h_{amb} -dependent correction factor on γ_{Vol} does not significantly polarize the estimation of the facies location. Nevertheless, this aspect could be taken into account for a future refinement of the proposed method, by iterating the classification algorithm twice and introducing a different h_{amb} -dependent correction factor for each of the estimated snow facies location at the first step.

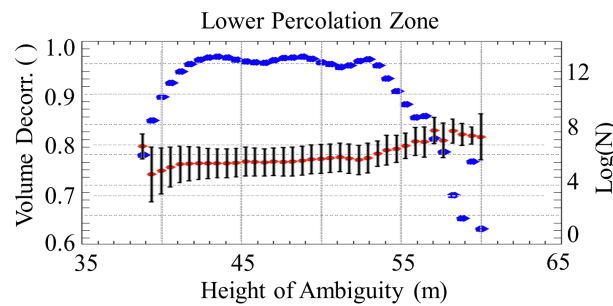


Figure 13. Dependency of the volume correlation factor γ_{Vol} on the height of ambiguity h_{amb} for the snow facies 3. Red dots: γ_{Vol} mean values, vertical black lines: γ_{Vol} standard deviations (axis on the left-hand side), blue dots: number of available γ_{Vol} samples N per h_{amb} interval in logarithmic scale (axis on the right-hand side).

6. Estimation of the Penetration Depth

Knowing the properties and the location of the different facies of the Greenland Ice Sheet represents the bases for further scientific investigations. In this section, we derive a map of the penetration depth, based on the model presented by Weber Hoen and Zebker in [9] and we compare it to real elevation measurements from TanDEM-X data. By assuming a homogeneous, lossy scattering medium, they modeled the volume correlation factor γ_{Vol} with respect to the one-way power penetration depth d_{1w} as:

$$\gamma_{Vol} = \frac{1}{\sqrt{1 + \left(\frac{2\pi\sqrt{\varepsilon}d_{1w}B_{\perp}}{r\lambda \tan\theta}\right)^2}} \quad (17)$$

where ε is the dielectric constant and, for an icy medium, it is supposed to be real and to remain constant throughout it. d_{1w} represents the penetration depth where the one-way power decreases by $1/e$. By inverting (17), we obtain d_{1w} as:

$$d_{1w} = \frac{r\lambda \tan\theta}{2\pi\sqrt{\varepsilon}B_{\perp}} \sqrt{\frac{1}{\gamma_{Vol}^2} - 1} \quad (18)$$

The two-way penetration depth d_{2w} can then be derived as:

$$d_{2w} = \frac{d_{1w}}{2} \quad (19)$$

We consider the two-way penetration depth because it is the one that approximates the location of the radar mean phase center and is therefore related to the measured interferometric height.

By exploiting the snow facies map in Figure 9a, we can now associate to facies with a proper value of ε . The dielectric constant ε can be related to the snow density ρ as presented in [43]; taking the single measurements which relate the density to the permittivity in H polarization, we performed a 2nd-order polynomial fitting, shown in Figure 14. Assuming a homogenous density of snow within the most superficial layers of the snow pack (until about 10 m depth), the mean snow density $\bar{\rho}$ along the EGIG line, accumulated over the period of spring 2004 to summer 2006, can be extrapolated from Equation (20) in [40] and associated to the different test sites, depending on the distance from T05 (as in Table 1 of [40]), leading to the following values:

- at T05 (belonging to facies 4): $\bar{\rho} = 0.41 \text{ g/cm}^3$,
- at T09 (belonging to facies 3): $\bar{\rho} = 0.40 \text{ g/cm}^3$,
- at T12 and T15 (belonging to facies 2): $\bar{\rho} = 0.40 \text{ g/cm}^3$ and $\bar{\rho} = 0.39 \text{ g/cm}^3$,
- from T21 to the summit of the traverse (belonging to facies 1): $\bar{\rho}$ decreases from about 0.38 g/cm^3 to about 0.33 g/cm^3 .

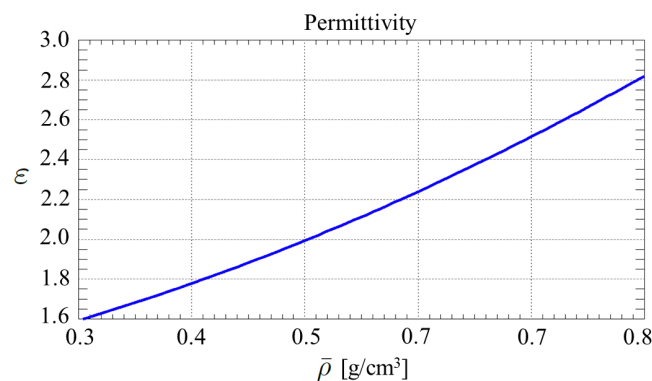


Figure 14. Relation between snow density and permittivity, derived from [43].

When more than a single $\bar{\rho}$ value per facies are available, the mean value has been considered. These values are summarized in Table 5, together with the corresponding permittivities. By substituting the derived ε into Equations (18) and (19), together with the other parameters derived for the considered TanDEM-X acquisitions, we obtain the map of the two-way penetration depth in Figure 15a. The corresponding histograms for each facies are depicted in Figure 16a and the mean value $E[d_{2w}]$ and standard deviation $\sigma_{d_{2w}}$ for each distribution are summarized in Table 6.

The obtained results over facies 1 (characterized by dry snow) match very well with the ones obtained by Rott et al. in [14], where a one-way penetration depth of 8.1 m at 10 GHz was estimated for dry, highly metamorphic snow, corresponding to a two-way penetration depth of 4.05 m.

Table 5. Mean snow density $\bar{\rho}$ and permittivity ε for the different snow facies of the Greenland Ice Sheet [40,43].

Facies	Mean Snow Density $\bar{\rho}$ (g/cm ³)	Permittivity ε
1	0.355	1.70
2	0.395	1.75
3	0.40	1.78
4	0.41	1.80

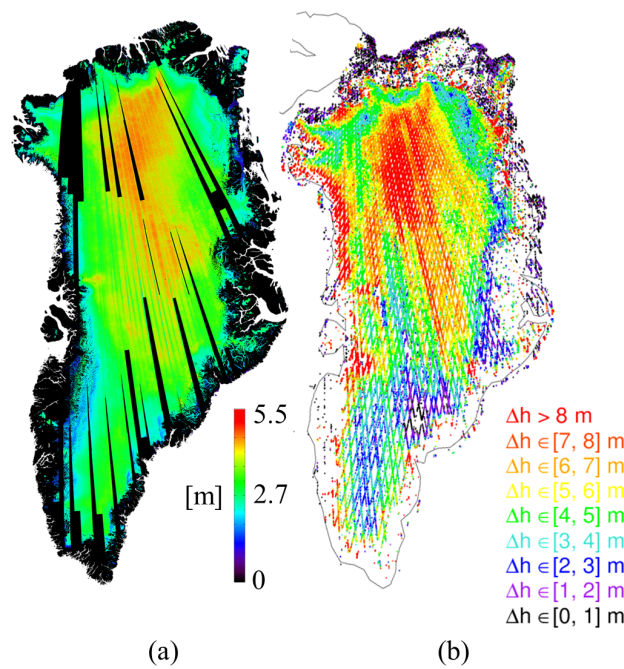


Figure 15. (a) Map of the retrieved X-band two-way penetration depth. (b) Mean differences between TanDEM-X DEM, acquired during winter, and ICESat measurements.

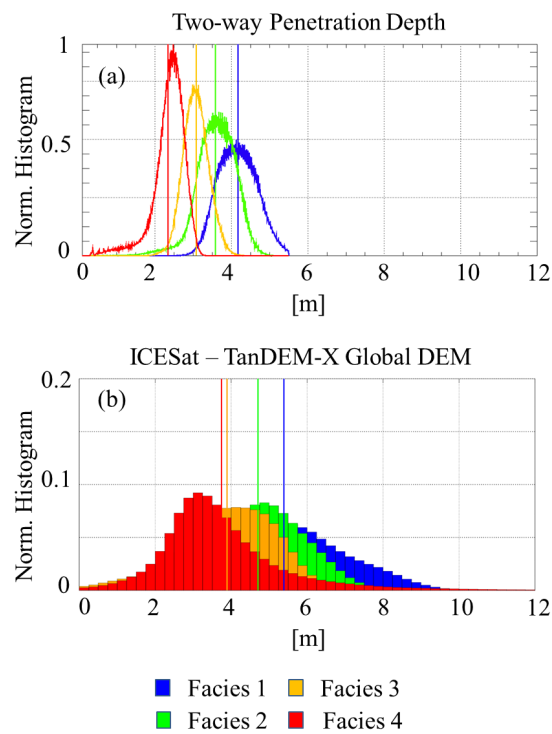


Figure 16. (a) Histograms of the two-way penetration depth for the different snow facies. (b) Histograms of the mean difference between ICESat and TanDEM-X DEM Δh for the different facies. The mean value of each distribution is indicated by a vertical line in the corresponding color.

Table 6. Mean values and standard deviations of the two-way penetration depth and of the difference between ICESat measurements and TanDEM-X (TDX) DEMs for the different snow facies. ΔH is the difference between the mean d_{2w} and the mean Δh .

Facies	Penetration Depth d_{2w}		ICESat-TDX DEM Δh		ΔH (m)
	Mean (m)	Std. Dev. (m)	Mean (m)	Std. Dev. (m)	
1	4.18	0.51	5.38	1.90	−1.20
2	3.58	0.56	4.70	1.49	−1.12
3	3.07	0.33	3.89	1.54	−0.82
4	2.34	0.49	3.74	2.32	−1.40

We also compared the obtained results to the difference between ICESat laser elevation measurements, carried out between 2003 and 2009 [44], and the final global TanDEM-X DEM. As already mentioned, radar DEMs typically represent the location of the mean phase center of the backscattered signal; in case of penetration into the snow pack, they will differ from ICESat, which measures the height of the surface. For each available ICESat value, we evaluated the mean difference Δh between ICESat and TanDEM-X DEM as:

$$\Delta h = E[h_{ICESat} - h_{TDX}] \quad (20)$$

where h_{TDX} identifies the mean height of the final TanDEM-X DEM within the considered ICESat footprint and h_{ICESat} represents the measured height from ICESat over the same ground area. The results are shown in Figure 15b.

Δh has been separately evaluated for the four different snow facies in Figure 9a by applying a defined polygon for each zone, derived as presented in Figure 9. The corresponding histograms for the different facies are depicted in Figure 16b and the mean values and standard deviations are again summarized in Table 6. It has to be mentioned that ICESat measurements are older than the considered TanDEM-X DEMs. In the time intermediate there have been changes in the height of the Ice Sheet that introduce a further amount of uncertainty in the estimation.

The depth of the mean phase center of a radar wave, measured by the interferometric phase, approximately equals the two-way penetration depth d_{2w} if the latter is lower than about 10% of the height of ambiguity h_{amb} , otherwise a bias between the two is introduced [45]. For the current analysis, the worst-case can be estimated using the ratio between the 3σ two-way penetration depth over the dry snow zone, given by $E[d_{2w}] + 3\sigma_{d_{2w}} \simeq 5.5$ m, and a minimum h_{amb} of about 40 m (Figure 13). The result is a ratio of about 14%, which allows us to reasonably assume that no significant bias is introduced between the two-way penetration depth d_{2w} and the elevation measurement Δh .

We can now evaluate the difference ΔH between the mean d_{2w} and the mean Δh for each snow facies as:

$$\Delta H = E[d_{2w}] - E[\Delta h] \quad (21)$$

Assuming a good accuracy of the two-way penetration depth d_{2w} , at least confirmed for the inner snow facies (characterized by the presence of dry snow) by the results obtained by Rott et al. in [14], ΔH is expected to be around zero. Even though the results match quite well, the obtained values, shown in Table 6, indicate the presence of a slightly negative offset which varies from about −0.8 m to −1.4 m.

A reason to at least partly explain such differences is the simplified (single layer) model of Hoen and Zebker for relating volume decorrelation to penetration depth. The model assumes that there is no depth dependency of the scattering cross-section, a constant density, and uncorrelated scatterers. This hypothesis is not true for a highly stratified medium such as polar firn, as addressed in Section 5.2 [39,40]. For example, since the penetration depth at X-band is on the order of a few meters, the density of the upper layers of the snow pack becomes of predominant importance. In particular, the first two meters typically present lower density than the mean values used here (see e.g., Figures 2

and 5 in [40]). If we now assume a decrease of 20% in snow density, which is comparable to the density change in the upper layers in [39,40] with respect to the mean one, this would result in an increase of the mean two-way penetration depth in the range from 7 cm (facies 1) up to 17 cm (facies 4), reducing the remaining offsets by the same amount.

Other sources of uncertainty may result from the fact that the TanDEM-X DEM has been calibrated using ICESat measurements in the outer regions of Greenland only. Along the Ice Sheet a self-adjusting block calibration has been implemented [46], which might also explain the persistence of a residual offset. A further reason might be the occurrence of height changes during the time span which separates ICESat measurements from TanDEM-X acquisitions.

A way to improve the accuracy of the penetration depth model could be to combine both backscatter and volume decorrelation information, which would be consistent with the applied snow facies classification method, which considers both quantities. This topic will be the object of further investigations.

7. Summary and Conclusions

In this paper we present an approach for locating different snow facies of the Greenland Ice Sheet by exploiting X-band TanDEM-X interferometric SAR acquisitions. We applied an unsupervised classification method based on the *c*-means fuzzy clustering algorithm, which uses features inherent in the data without subjective interference. This is an appropriate method for exploring the information content of the 2D feature space, given by the combination of radar backscatter γ^0 and volume correlation factor γ_{Vol} , with respect to glacier facies, which is a main objective of the work. The algorithm has been applied to TanDEM-X data acquired during winter 2010/2011, by analyzing three different partitions, obtained by selecting a different number of clusters ($c = 3, 4, 5$), in order to assess the feasibility for discriminating facies types. The partition composed of 4 clusters is a good compromise in terms of classification reliability and high level of detail and has therefore been chosen as reference for the current work. We then provided a statistical analysis of both γ^0 and γ_{Vol} over the Ice Sheet for each different facies and investigated the dependency of γ_{Vol} on the acquisition geometry and, in particular, on the height of ambiguity ranging from 40 m to 53 m. The use of a correction factor for γ_{Vol} depending on the height of ambiguity might represent a starting point for a future refinement of the classification algorithm.

The derived snow facies have been interpreted by means of reference melt data and in situ measurements along the EGIG line.

Facies 1 is dominated by the presence of dry snow. Further refined clustering reveals two sub-facies (a southern and a northern one) which can be related to different snow accumulation rates. Facies 2 to 4 belong to a transition zone where melt phenomena increase toward the outer regions of the Ice Sheet. Facies 2 and 3 approximately correspond to the percolation zone, and facies 4 to the wet snow zone, reported by Benson in [2]. This is confirmed by structural properties of the snow volume as observed by Morris and Wingham in [40]. The subdivision into different facies results from differences in γ^0 and γ_{Vol} due to spatial changes in microstructure of firn related to melt intensity and accumulation rates, which vary with elevation, snowfall pattern, and wind drift. The subdivision is therefore a pointer to such differences.

Given the high similarity in terms of backscattering properties and volume decorrelation among pixels belonging to the same cluster, we can then apply the mean value of snow density to the entire considered snow facies. This allowed us to estimate the penetration depth by inverting the interferometric model proposed by Weber Hoen and Zebker in [9] and assuming the dielectric constant for an icy medium to be real and to remain constant for a given facies type. The obtained results show a mean two-way penetration depth of 4.18 m for facies 1, 3.58 m for facies 2, 3.07 m for facies 3, and 2.34 m for facies 4. These values have been compared to the elevation between the global TanDEM-X DEM and ICESat measurements, proving that, theoretically, no considerable bias between the two measurement approaches is to be expected. A residual negative offset has nevertheless been

detected, which varies from about -0.8 m to -1.40 m for the different snow facies, which will be object of further investigations. A possible explanation might be the fact that the Weber Hoen and Zebker's model relies on simplifying assumptions, such as no depth dependency of the scattering cross-section, a constant density, and uncorrelated scatterers. Other sources of uncertainty may be related to the TanDEM-X DEM calibration or to the occurrence of height changes during the time span which separates ICESat measurements from TanDEM-X acquisitions.

Even though featuring a limited penetration into the snow pack, TanDEM-X interferometric data demonstrates itself to be highly sensitive to changes in snow properties and represents a highly valuable data set for investigating Greenland Ice Sheet characteristics and its evolution. The continuous monitoring of the cryosphere in an era of climate changes represents one of the most challenging tasks for the remote sensing community. The developed approach can also be applied to more recent TanDEM-X acquisitions over Greenland and Antarctica Ice Sheets, to characterize their properties and changes. The work performed here represents therefore a starting point for further analyzing the evolution in time of Ice Sheets, by monitoring the changes in the location of the different snow facies, as an indicator of climate changes. Moreover, the technique could be exploited within future interferometric SAR missions as well. For example, the Tandem-L mission is being currently designed for acting as single-pass interferometer at L-band [47], with the main object of assessing the dynamic processes in the Earth's environmental system.

Acknowledgments: The authors would like to thank the anonymous reviewers for their help to improve the quality of the paper.

Author Contributions: Paola Rizzoli performed the scientific analysis and prepared the manuscript. Michele Martone provided the difference map between TanDEM-X DEM and ICESat and the corresponding statistical analysis. Paola Rizzoli and Michele Martone processed the TanDEM-X data. Helmut Rott contributed to the scientific interpretation of the obtained results. Alberto Moreira and Helmut Rott contributed to the definition of the developed algorithms. All authors contributed to editing and reviewing the manuscript.

Conflicts of Interest: The authors declare no conflict of interest.

References

1. Groh, A.; Ewert, H.; Fritsche, M.; Rülke, A.; Rosenau, R.; Scheinert, M.; Dietrich, R. Assessing the Current Evolution of the Greenland Ice Sheet by Means of Satellite and Ground-Based Observations. *Surv. Geophys.* **2014**, *35*, 1259–1480.
2. Benson, C.S. *Stratigraphic Studies in the Snow and Firn of the Greenland Ice Sheet*; Research Report 70; Reprinted August 1996; U.S. Army Snow, Ice and Permafrost Research Establishment: Hanover, Germany, 1962.
3. Bales, R.C.; Guo, Q.; Shen, D.; McConnell, J.R.; Du, G.; Burkhart, J.F.; Spikes, V.B.; Hanna, E.; Cappelen, J. Annual Accumulation for Greenland Updated using Ice Core Data developed during 2000/2006 and Analysis of Daily Coastal Meteorological Data. *J. Geophys. Res.* **2009**, *114*, 1–14.
4. Munk, J.; Jezek, K.C.; Foster, R.R.; Gogineni, S. An Accumulation Map for the Greenland Dry-Snow Facies Derived from Spaceborne Radar. *J. Geophys. Res.* **2003**, *108*, doi:10.1029/2002JD002481.
5. Jezek, K.G.; Gogineni, P.; Shanableh, M. Radar Measurements of Melt Zones on the Greenland Ice Sheet. *Geophys. Res. Lett.* **1994**, *21*, 33–36.
6. Rignot, E.; Jezek, K.; van Zyl, J.; Drinkwater, M. Radar Scattering from Snow Facies of the Greenland Ice Sheet: Results from the AIRSAR 1991 Campaign. In Proceedings of the IEEE IGARSS, Tokyo, Japan, 18–21 August 1993; pp. 1270–1272.
7. Ashcraft, I.; Long, D. Observation and Characterization of Radar Backscatter Over Greenland. *IEEE TGRS* **2005**, *43*, 225–237.
8. Joughin, I.; Smith, B.E.; Howat, I.M.; Moon, T.; Scambos, T.A. A SAR Record of Early 21st Century Change in Greenland. *J. Glaciol.* **2016**, *62*, 62–71.
9. Weber Hoen, E.; Zebker, H. Penetration Depths Inferred from Interferometric Volume Decorrelation Observed over the Greenland Ice Sheet. *IEEE TGRS* **2000**, *38*, 2571–2583.
10. Krieger, G.; Moreira, A.; Fiedler, H.; Hajnsek, I.; Werner, M.; Younis, M.; Zink, M. TanDEM-X: A Satellite Formation for High Resolution SAR Interferometry. *IEEE TGRS* **2007**, *45*, 3317–3341.

11. Krieger, G.; Zink, M.; Bachmann, M.; Bräutigam, B.; Schulze, D.; Martone, M.; Rizzoli, P.; Steinbrecher, U.; Antony, J.W.; De Zan, F.; et al. TanDEM-X: A Radar Interferometer with Two Formation-Flying Satellites. *Acta Astronaut.* **2013**, *89*, 83–98.
12. Zink, M.; Bachmann, M.; Bräutigam, B.; Fritz, T.; Hajnsek, I.; Krieger, G.; Moreira, A.; Wessel, B. TanDEM-X: The New Global DEM Takes Shape. *IEEE GRSM* **2014**, *2*, 8–23.
13. Martone, M.; Bräutigam, B.; Krieger, G. Decorrelation Effects in Bistatic TanDEM-X Data. In Proceedings of the IEEE IGARSS, Munich, Germany, 22–27 July 2012; pp. 5558–5561.
14. Rott, H.; Sturm, K.; Miller, H. Active and Passive Microwave Signatures of Antarctic Firn by Means of Field Measurements and Satellite Data. *Ann. Glaciol.* **1993**, *17*, 337–343.
15. Rott, H.; Floricioiu, D.; Wuite, J.; Scheiblauer, S.; Nagler, T.; Kern, M. Mass Changes of Outlet Glaciers along the Nordensjøkold Coast, Northern Antarctic Peninsula, Based on TanDEM-X Satellite Measurements. *Geophys. Res. Lett.* **2014**, *41*, 8123–8129.
16. Munk, J.; Jezek, K.; Baumgartner, F.; Gogineni, S.P.; Forster, R.R.; Zabel, I.H.H. Estimating a Volumetric Backscatter Coefficient from In-situ Measurements on the Greenland Ice Sheet. In Proceedings of the IEEE IGARSS, Honolulu, HI, USA, 24–28 July 2000; pp. 917–919.
17. Rizzoli, P.; Martone, M.; Bräutigam, B. Greenland Snow Facies Identification Approach using TanDEM-X Interferometric Data. In Proceedings of the IEEE IGARSS, Milan, Italy, 26–31 July 2015; pp. 2060–2063.
18. Bezdek, J.; Ehrlich, R.; Full, W. FCM: The Fuzzy *c*-Means Clustering Algorithm. *Comput. Geosci.* **1984**, *10*, 191–203.
19. Partington, K.C. Discrimination of Glacier Facies using Multi-Temporal SAR Data. *J. Glaciol.* **1998**, *44*, 42–53.
20. Tran, N.; Rémy, F.; Feng, H.; Féménias, P. Snow Facies Over Ice Sheets Derived From Envisat Active and Passive Observation. *IEEE TGRS* **2008**, *46*, 3694–3708.
21. Höppner, F.; Klawonn, F.; Kruse, R.; Runkler, T. *Fuzzy Cluster Analysis: Methods for Classification, Data Analysis and Image Recognition*; Wiley: New York, NY, USA, 1999.
22. Miyamoto, S.; Ichihashi, H.; Honda, K. *Algorithms for Fuzzy Clustering: Methods in *c*-Means Clustering with Applications*; Springer Science & Business Media: Berlin, Germany, 2008.
23. Derrig, R.A.; Ostaszewski, K.M. Fuzzy Techniques of Pattern Recognition in Risk and Claim Classification. *J. Risk Insur.* **1995**, *62*, 447–482.
24. Das, S.; Baruah, H.K. Application of Fuzzy C-Means Clustering Technique in Vehicular Pollution. *J. Process Manag. New Technol.* **2013**, *1*, 96–107.
25. Goyal, M.; Kumar, S. Improving the Initial Centroids of k-means Clustering Algorithm to Generalize its Applicability. *J. Inst. Eng. Ser. B* **2014**, *95*, 345–350.
26. Fritz, T.; Rossi, C.; Yague-Martinez, N.; Rodriguez-Gonzalez, F.; Lachaise, M.; Breit, H. Interferometric Processing of TanDEM-X data. In Proceedings of the IEEE IGARSS, Vancouver, BC, Canada, 24–29 July 2011; pp. 2428–2431.
27. Rizzoli, P.; Bräutigam, B. Radar Backscatter Modeling Based on Global TanDEM-X Mission Data. *IEEE TGRS* **2013**, *52*, 5974–5988.
28. Rizzoli, P.; Martone, M.; Bräutigam, B. Global Interferometric Coherence Maps From TanDEM-X Quicklook Data. *IEEE GRSL* **2014**, *11*, 1861–1865.
29. Raney, R.K.; Freeman, T.; Hawkins, R.W.; Bamler, R. A Plea for Radar Brightness. In Proceedings of the IEEE IGARSS, Pasadena, CA, USA, 8–12 August 1994; pp. 1090–1092.
30. Martone, M.; Rizzoli, P.; Bräutigam, B.; Krieger, G. A Method for Generating Forest/Non-Forest Maps from TanDEM-X Interferometric Data. In Proceedings of the IEEE IGARSS, Milan, Italy, 26–31 July 2015; pp. 2634–2637.
31. Martone, M.; Bräutigam, B.; Krieger, G. Quantization Effects in TanDEM-X Data. *IEEE TGRS* **2015**, *53*, 583–597.
32. Citterio, M.; Ahlstrom, A. The Aerophotogrammetric Map of Greenland Ice Masses. *Cryosphere* **2013**, *7*, 445–449.
33. Tedesco, M. *Greenland Daily Surface Melt 25km EASE-Grid; Data from 1979 to 2010*; Digital Media, City College of New York, The City University of New York: New York, NY, USA, 2010.
34. Nghiem, S.V.; Hall, D.K.; Mote, T.L.; Tedesco, M.; Albert, M.R.; Keegan, K.; Shuman, C.A.; DiGirolamo, N.E.; Neumann, G. The Extreme Melt Across the Greenland Ice Sheet in 2012. *Geophys. Res. Lett.* **2012**, *39*, doi:10.1029/2012GL053611.

35. Nilsson, J.; Vallelonga, P.; Simonsen, S.B.; Sandberg Sørensen, L.; Forsberg, R.; Dahl-Jensen, D.; Hirabayashi, M.; Goto-Azuma, K.; Hvidberg, C.S.; Kjær, H.A.; et al. Greenland 2012 Melt Event Effects on CryoSat-2 Radar Altimetry. *Geophys. Res. Lett.* **2015**, *42*, 3919–3926.
36. BYU Center for Remote Sensing; NASA Jet Propulsion Laboratory (JPL); European Space Agency (ESA) Advanced Scatterometer (ASCAT) Sigma-0 Browse Images (Non-Enhanced). Scatterometer Climate Record Pathfinder. Available online: http://www.scp.byu.edu/data/Ascatt/SigBrw/ASCAT_SigBrw.html (accessed on 7 March 2017).
37. The International Glaciological Expedition to Greenland (EGIG), 1956–74. *Polar Rec.* **1975**, *110*.
38. Wingham, D.J. CryoSat: A Mission to Determine Fluctuations in the Earth's Ice Fields. In Proceedings of the IEEE IGARSS, Toronto, ON, Canada, 24–28 June 2002; pp. 1750–1752.
39. Scott, J.B.T.; Nienow, P.; Mair, D.; Parry, V.; Morris, E.; Wingham, D.J. Importance of Seasonal and Annual Layers in Controlling Backscatter to Radar Altimeter across the Percolation Zone of an Ice Sheet. *Geophys. Res. Lett.* **2006**, *33*, 1–6.
40. Morris, E.M.; Wingham, D.J. The Effect of Fluctuations in Surface Density, accumulation and Compaction on Elevation Changes along the EGIG Line, Central Greenland. *J. Glaciol.* **2011**, *57*, 416–430.
41. Scott, J.B.T.; Mair, D.; Nienow, P.; Parry, V.; Morris, E.M. A Ground-Based Radar Backscatter Investigation in the Percolation Zone of the Greenland Ice Sheet. *Remote Sens. Environ.* **2006**, *104*, 361–373.
42. Flach, J.; Partington, K.; Ruiz, C.; Jeansou, E.; Drinkwater, M. Inversion of the Surface Properties of Ice Sheets from Satellite Microwave Data. *IEEE TGRS* **2005**, *43*, 743–752.
43. Fujita, S.; Hirabayashi, M.; Goto-Azuma, K.; Dallmayr, R.; Satow, K.; Zheng, J.; Dahl-Jensen, D. Densification of Layered Firn of the Ice Sheet at NEEM, Greenland. *J. Glaciol.* **2014**, *60*, 905–921.
44. National Snow and Ice Data Center (NSIDC) GLAS/ICESat L2 Global Land Surface Altimetry Data, Version 34. Available online: <http://dx.doi.org/10.5067/ICESAT/GLAS/DATA227> (accessed on 7 March 2017).
45. Dall, J. InSAR Elevation Bias Caused by Penetration Into Uniform Volumes. *IEEE TGRS* **2007**, *45*, 2319–2324.
46. Wessel, B.; Bertram, A.; Gruber, A.; Bemm, S.; Dech, S. A New High-Resolution Elevation Model of Greenland Derived from TanDEM-X. In Proceedings of the ISPRS Annals of the Photogrammetry, Remote Sensing and Spatial Information Sciences of the XXIII ISPRS Congress, Prague, Czech Republic, 12–19 July 2016; pp. 9–16.
47. Moreira, A.; Krieger, G.; Hajnsek, I.; Papathanassiou, K.; Younis, M.; Lopez-Dekker, P.; Huber, S.; Villano, M.; Pardini, M.; Eineder, M.; et al. Tandem-L: A Highly Innovative Bistatic SAR Mission for Global Observation of Dynamic Processes on the Earth's Surface. *IEEE Geosci. Remote Sens. Mag.* **2015**, *3*, 8–23.



© 2017 by the authors. Licensee MDPI, Basel, Switzerland. This article is an open access article distributed under the terms and conditions of the Creative Commons Attribution (CC BY) license (<http://creativecommons.org/licenses/by/4.0/>).